RSC Advances

PAPER

View Article Online
View Journal | View Issue

Cite this: *RSC Adv.*, 2025, **15**, 37273

Transdermal delivery of near-infrared photothermal-responsive PDA@Ag through dissolvable carboxymethyl chitosan films coated on PEGDA microneedle arrays for potential antibacterial applications

Ya Gao, †*[a] Haoping Huo,†[a] Jianlin Li,[b] Nengqing Wang,[a] Haonan Gao[a] and Yingbo Wang *[a]

Eradicating cutaneous infections induced by pathogenic microorganisms, such as bacteria, fungi, and viruses, *via* conventional topical drug delivery is challenging owing to limited epidermal penetration. To overcome this limitation, we fabricated a poly(ethylene glycol) diacrylate (PEGDA) microneedle array coated with a carboxymethyl chitosan (CMC) film embedded within situ-synthesized polydopamine-modified silver nanoparticles (PDA@Ag NPs) for enhanced antibacterial efficacy. This design utilizes microneedle (MN)-mediated skin perforation to enhance drug permeation, combined with rapid film dissolution for the efficient release of the payload. The experimental findings revealed that the PDA@Ag-CMC/PEGDA MNs possess favorable biocompatibility along with dual photothermal and photodynamic functionalities. Mild photothermal therapy (PTT) triggered by these MNs promotes the production of antibacterial reactive oxygen species (ROS), resulting in a high antibacterial rate of up to 98% against both *Escherichia coli* (*E. coli*) and *Staphylococcus aureus* (*S. aureus*) under NIR irradiation at a PDA@Ag concentration of 40 μg mL^{-1}. To assess transdermal delivery performance, lidocaine hydrochloride (LiH) (78 μg per MN array) was incorporated into the CMC film as a model drug. Physiological conditions confirmed accelerated LiH release from the PDA@Ag-LiH-CMC/PEGDA system upon aqueous exposure. This minimally invasive approach demonstrated promising broad-spectrum antibacterial activity, suggesting that the PDA@Ag-LiH-CMC/PEGDA platform could serve as a viable clinical solution for managing polymicrobial skin infections and alleviating wound pain.

Received 13th June 2025
Accepted 15th September 2025

DOI: 10.1039/d5ra04189a

rsc.li/rsc-advances

1 Introduction

The treatment of bacterial infections is one of the most challenging issues in healthcare worldwide. Although antibiotics are the primary treatment for bacterial infections, their overuse and misuse have accelerated the emergence of bacterial resistance, posing a serious threat to clinical therapeutic outcomes. Therefore, highly efficient alternative therapeutic strategies that do not induce multidrug resistance need to be developed.[1–7] Various novel antibacterial strategies have been developed, including antibacterial materials (such as quaternary ammonium salts, metal ions, and hydrogels) and non-antibiotic approaches such as immunotherapy, photothermal therapy (PTT), and photodynamic therapy (PDT).[8–10] Among these, PTT has received significant attention because of its controllable nature, minimal side effects, and low propensity to induce resistance.[11] Specifically, near-infrared (NIR)-responsive PTT, with its deep tissue penetration ability and precise photothermal conversion characteristics, can generate localized hyperthermia to effectively eradicate bacteria while avoiding systemic toxicity, making it a promising alternative to antibiotics.[12,13]

Microneedles (MNs) are innovative drug delivery systems composed of micron-scale needle arrays that can painlessly penetrate the stratum corneum to form microchannels, allowing precise drug delivery to target sites.[14–16] Photothermal agent-loaded MNs can disrupt biofilms, increase the diffusion of antibacterial agents, and effectively target deep-seated drug-resistant bacteria, making them highly efficient tools for treating skin infections.[17–20] Various types of photothermal agents have been developed, including polydopamine (PDA), inorganic nanoparticles (NPs) (*e.g.*, copper sulfide NPs and carbon-based NPs), and indocyanine green.[21–23] Among these materials, PDA has excellent biocompatibility and degradability. It also has photothermal antibacterial properties under 808 nm NIR light

[a]*School of Chemistry and Chemical Engineering, Xinjiang Normal University, Urumqi, 830054, China. E-mail: 1965810837@qq.com; ybwang20002575@163.com*
[b]*Academic Conference Center, Inner Mongolia University, Hohhot, 010021, China*
† Authors contributed equally.

irradiation, effectively inhibiting bacterial proliferation and reducing the risk of skin infections. However, the limited NIR absorption of PDA alone greatly hinders its clinical application. To achieve enhanced photothermal performance, researchers have incorporated inorganic NPs to form composite materials. For example, Gao *et al.* reported that loading copper NPs onto PDA surfaces *via* reduction-deposition methods increased the photothermal conversion efficiency to 57.8%, achieving an antibacterial rate exceeding 99%.[24] Zhang *et al.* reported that gold nanorods (AuNRs) and hollow copper sulfide (CuS) can be integrated with PDA *via* electrostatic self-assembly, forming a core–shell structure that significantly improves the light absorption efficiency of PDA.[25] These studies confirmed that PDA-based composites loaded with inorganic NPs have superior photothermal antibacterial performance.

Silver (Ag) NPs are potent and broad-spectrum antibacterial agents capable of effectively eradicating Gram-negative and Gram-positive bacterial strains and fungal species. They specifically affect viral pathogens while exhibiting a lower propensity for inducing resistance. Their antibacterial mechanisms involve accumulating on bacterial membrane surfaces, leading to structural disruption and an increase in permeability, which results in cell death.[26–29] The released Ag^+ ions can interfere with bacterial metabolism; however, excessive Ag^+ concentrations may elicit cytotoxicity and tissue damage.[30,31] Controlling Ag^+ concentrations to ensure biosafety while achieving rapid bactericidal action remains a critical challenge. Dai *et al.* embedded Ag NPs in an alginate hydrogel and used the porous structure of the hydrogel for the sustained release of Ag^+, thereby achieving a seven-day (long-term) antibacterial effect with minimal cytotoxicity.[32] Chokesawatanakit *et al.* developed a photocatalytic system involving TiO_2 nanotubes loaded with Ag^+, where UV light irradiation induces reactive oxygen species (ROS) production by TiO_2, synergizing with Ag^+ to disrupt bacterial membranes. A balance between efficient antibacterial activity and biosafety was achieved at low concentrations of Ag^+.[33] Additionally, based on the metal chelation properties of phenolic hydroxyl/amine groups on the surface of PDA or electrostatic adsorption for loading inorganic NPs, we performed *in situ* reduction of nanosilver by PDA to fabricate photothermal antibacterial PDA@Ag composites. These composites can disrupt microbial cell membrane structures, inhibit biofilm formation, and induce ROS accumulation, thereby reducing microbial activity and promoting apoptosis.[34–36] Therefore, PDA@Ag NPs may serve as effective agents in photothermal antibacterial therapy.

In this study, poly(ethylene glycol) diacrylate (PEGDA) was used as the foundational material for MN fabrication because it has exceptional mechanical robustness and adjustable crosslinking properties. Carboxymethyl chitosan (CMC), a highly water-soluble chitosan derivative, was incorporated for its notable therapeutic benefits, which include enhanced wound repair, hemostatic capability, scar prevention, pain relief, and antibacterial efficacy. Owing to its excellent biocompatibility and biodegradability, CMC has extensive applications in the biomedical field.[37–41] In this study, we used a UV-induced polymerization method to fabricate CMC films coated with PEGDA MNs (CMC/PEGDA). The composite MNs (PDA@Ag-CMC/PEGDA) were prepared *via* UV light-induced polymerization. Dopamine (DA) was polymerized to form PDA in a weakly basic environment, and PDA subsequently reduced silver ions *in situ* at room temperature to form a metallic phenolic network structure, resulting in the formation of particulate PDA@Ag under centrifugal force (Scheme 1).[42,43] The PDA@Ag NPs were further incorporated into the CMC coating on the surface of the PEGDA MNs. After skin insertion, the CMC coating on the MNs dissolved, releasing the PDA@Ag NPs. Following exposure to 808 nm NIR light (after the MN array was applied to the skin), the MN patch itself was left in place during the subsequent NIR irradiation procedure to ensure consistent and uniform light exposure. The PDA@Ag composite exhibited a pronounced photothermal effect, causing localized hyperthermia (~50 °C). This thermal effect increases the permeability of the bacterial membrane while simultaneously producing significant amounts of ROS, resulting in oxidative stress that enables combined photothermal (PTT) and photodynamic (PDT) antibacterial effects. To evaluate MN-mediated drug stability, we incorporated lidocaine hydrochloride (LiH), a clinically used local anesthetic, as a model compound in the PDA@Ag-LiH-CMC/PEGDA MN system. We examined the effects of hyperthermic conditions during photothermal antibacterial treatment on the activity of LiH. The results indicated that photothermal treatment at ~50 °C slightly affected the stability of LiH, suggesting that the synthesis of the composite MNs was relatively mild. The antibacterial efficacy of the photothermally active MNs was evaluated against Gram-positive (*S. aureus*) and Gram-negative (*E. coli*) bacterial strains. These findings serve as a platform for designing more functional PEGDA-based MN systems with broad-spectrum antibacterial applications.

2 Experimental section

2.1. Materials

Silver nitrate ($AgNO_3$) was purchased from Tianjin Shengao Chemical Reagent Co., Ltd (China). DA, ammonium hydroxide solution (25–28 wt%), rhodamine B (RhB), and glucose were purchased from Sigma-Aldrich and Tianjin Zhiyuan Chemical Reagent Co., Ltd (China), respectively. Absolute ethanol was purchased from Sichuan Xilong Scientific Co., Ltd (China), while carboxymethyl chitosan (CMC) was purchased from Shanghai YuanYe Biotechnology Co., Ltd (China). Poly(ethylene glycol) diacrylate (PEGDA, M_n = 250), 2-hydroxy-2-methylpropiophenone (HMP) agarose, and polydimethylsiloxane (PDMS) were purchased from Shanghai Macklin Biochemical Co., Ltd (China). LiH and 1,3-diphenylisobenzofuran (DPBF, 97%) were purchased from Shanghai Aladdin Biochemical Technology Co., Ltd (China). *S. aureus* (SA, ATCC 25923) and *E. coli* (EC, ATCC 25922) were obtained from the American Type Culture Collection (ATCC, USA). Dulbecco's modified Eagle's medium (DMEM), fetal bovine serum (FBS), penicillin-streptomycin solution, murine fibroblasts (L929), Luria-Bertani (LB) broth, and phosphate-buffered saline (PBS) were purchased from Wuhan Sevier Biological Technology Co., Ltd (China). A bacterial viability assay

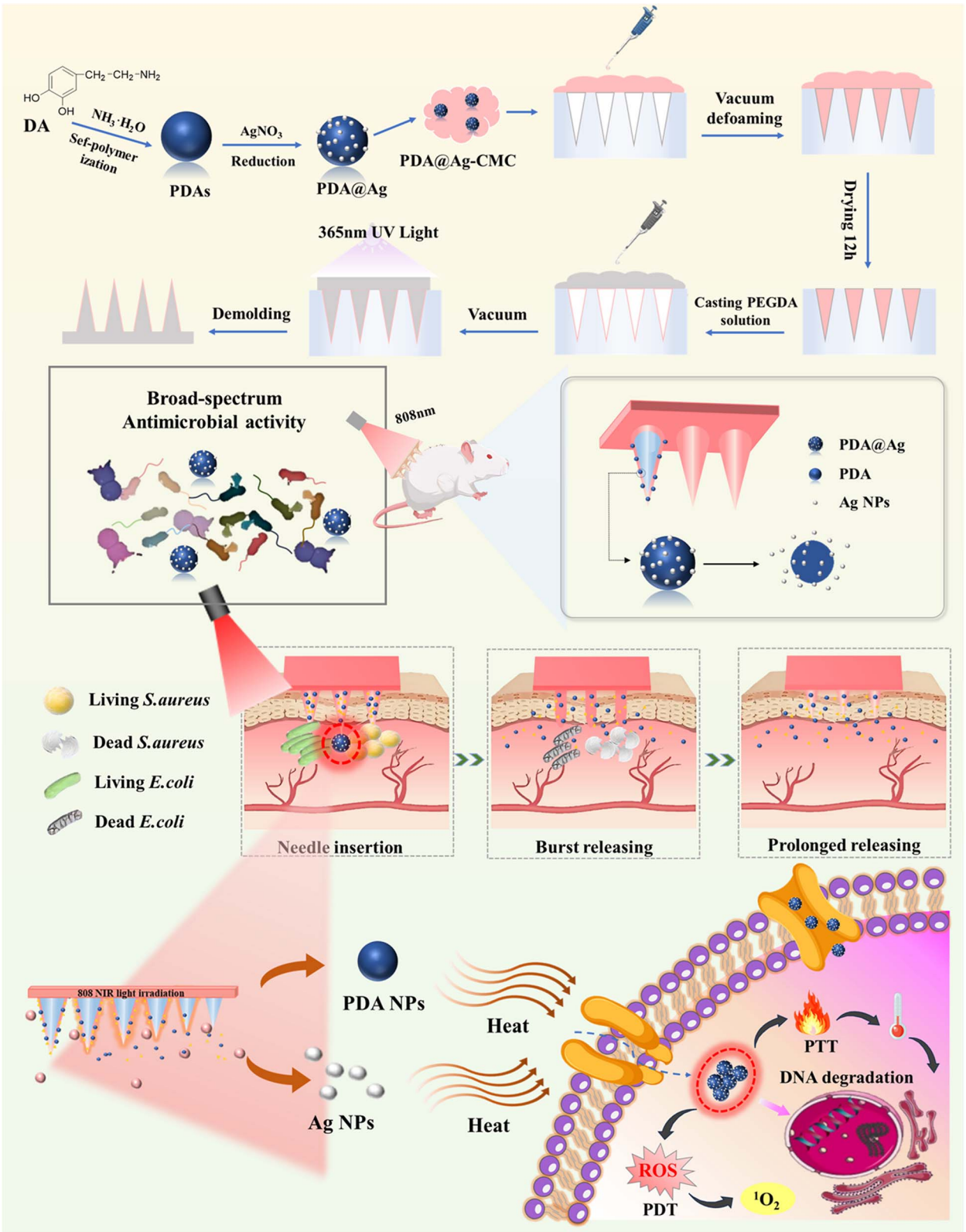

Scheme 1 Schematic illustration of the application of the PDA@Ag-CMC/PEGDA MN patch onto the skin and the procedure used to fabricate the PEGDA-based microneedle substrate.

kit (DMAO/PI) was purchased from Beyotime Biotechnology (China). Female BALB/c mice were purchased from Chengdu Daxiao Biotech Co., Ltd (China).

2.2. Preparation of PDA

Solution 1 was prepared by homogenizing 0.6 mL of ammonium hydroxide (25 wt%) with 90 mL of deionized water and 40 mL of

absolute ethanol under magnetic stirring (30 min, 25 °C). Solution 2 was formulated by dissolving 0.5 g of dopamine hydrochloride in 10 mL of deionized water. The latter solution was introduced dropwise into solution 1 under vigorous stirring, and the reaction proceeded for 24 h at ambient temperature. The resulting suspension was centrifuged (12 000 rpm, 8 min) to collect the PDA NPs, which were then purified *via* five cycles of washing with deionized water and drying for subsequent use.

2.3. Preparation of PDA@Ag NPs

The PDA@Ag nanocomposites were synthesized by combining 20 mL of $AgNO_3$ aqueous solution (5 mg mL^{-1}), 20 mL of $NH_3 \cdot H_2O$ (25 wt%), 40 mL of glucose solution (10 mg mL^{-1}), and 10 mL of freshly prepared PDA suspension under continuous magnetic stirring (500 rpm, 8 h).[36] The product formed was isolated *via* centrifugation (12 000 rpm, 10 min), followed by washing three times with deionized water to remove impurities. Finally, the purified PDA@Ag NPs were dried and stored for subsequent characterization and applications.

2.4. Characterization of PDA@Ag

The nanostructural features of PDA@Ag were characterized *via* high-resolution scanning electron microscopy (SEM; LEO-1430VP, Germany) and transmission electron microscopy (TEM; H-7650, Hitachi, Japan). Colloidal properties, including hydrodynamic diameter and surface charge, were measured *via* dynamic light scattering (DLS) at 25 °C (Zetasizer Nano ZS90, Malvern Instruments, UK). X-ray photoelectron spectroscopy (XPS; Thermo Fisher Nexsa) was performed to determine the chemical state of the silver species. Crystallographic analysis was performed *via* X-ray diffraction (XRD; D2-PHASER, BRUKER, Germany), whereas molecular interactions were investigated *via* Fourier transform infrared spectroscopy (FTIR; VERTEX70, BRUKER, Germany). Optical absorption properties were examined using UV-vis-NIR spectroscopy (TU-1901, Agilent). Quantitative elemental analysis was conducted *via* inductively coupled plasma-optical emission spectrometry (ICPOES 730, Agilent). The ROS generation capacity was evaluated through electron spin resonance spectroscopy (ESR; A300, BRUKER) to detect hydroxyl ($^{\bullet}OH$) and superoxide ($^{\bullet}O_2^-$) radicals. The microstructure of the microneedles was characterized using high-resolution confocal laser scanning microscopy (CLSM, Leica SP8, Germany). The depth of microneedle penetration into the skin was observed using a slide scanner (3DHISTECH, Pannoramic MIDI, Hungary).

2.5. Preparation of PDA@Ag-LiH-CMC/PEGDA MNs

A PDMS mixture with a curing agent (10 : 1 ratio) was applied to the surface of a stainless steel main needle template (Zhen Zhou, China). The mixture was then vacuum degassed for 1 h, cured at 70 °C for 2 h, and gently detached to obtain a PDMS mold. PDA@Ag NPs (10 μg, 20 μg, and 40 μg) were uniformly dispersed in 1 mL of a 3% CMC solution, and 200 μL of this PDA@Ag-CMC solution was placed on the PDMS mold. The sample was vacuum-treated for 15 min at room temperature to remove excess liquid, and then the PDMS mold was dried at room temperature for 12 h to form a PDA@Ag-CMC coating on the inner surface. Subsequently, 150 μL of a PEGDA solution containing 0.5 wt% HMP was added to the PDMS mold with the PDA@Ag-CMC coating, vacuum-treated for 30 min, and exposed to UV light (365 nm wavelength) for 30 s. The mold was then gently peeled off to obtain PDA@Ag-CMC-coated PEGDA MNs (PDA@Ag-CMC/PEGDA MNs), which were stored at 4 °C for further use. To evaluate the drug delivery ability of the MNs, LiH was used as a model drug. Specifically, 0.081 g of LiH was incorporated into the CMC coating,[44] and PDA@Ag-LiH-CMC/PEGDA MNs were prepared using the same method.

2.6. Photothermal performance

The photothermal properties of PDA@Ag were assessed by irradiating three sample groups, which included the PBS (control), PDA (40 μg mL^{-1}), and PDA@Ag (40 μg mL^{-1}) groups, in colorimetric dishes with an 808 nm NIR laser at 1.5 W cm^{-2}. To investigate the power-dependent effects, PDA@Ag NPs (40 μg mL^{-1}) were exposed to different irradiation intensities ranging from 0.5 to 2.0 W cm^{-2} (0.5, 1.0, 1.5, and 2.0 W cm^{-2}). Concentration-dependent photothermal behavior was studied by testing PDA@Ag solutions at 0, 10, 20, and 40 μg mL^{-1} concentrations under fixed NIR conditions (808 nm, 1.5 W cm^{-2}). The temperature variations were continuously monitored using a CEM infrared thermal camera (China). The photothermal stability was evaluated through five consecutive heating–cooling cycles under identical experimental parameters. The photothermal conversion efficiency was quantitatively determined by applying thermodynamic eqn (1)–(3) to the obtained temperature profiles.

$$\eta = \frac{hA(\Delta T_{max,min} \cdot \Delta T_{max,H_2O})}{I \cdot (1 - 10^{-A\lambda})} \quad (1)$$

$$t = -\frac{mC}{hA \ln(\theta)} \quad (2)$$

$$\theta = \frac{\Delta T}{\Delta T(\mathrm{mix,max})} \quad (3)$$

In this context, η represents the photothermal conversion efficiency, h represents the heat transfer coefficient, A represents the surface area of the container, t represents the natural cooling duration, ΔT_{max}, min represents the maximal temperature variation between the PDA@Ag solution (40 μg mL^{-1}) after 10 min and its initial temperature, $\Delta T_{max,H_2O}$ represents the highest temperature differential between the PBS solution at 10 min and its starting temperature, m and C represent the mass and specific heat capacity of PBS, respectively, ΔT represents the temperature deviation from the baseline during cooling, and I represents the output power of the infrared laser. For the computational procedure, the hA value was initially derived from the linear correlation between t and $-\ln(\theta)$, which was subsequently incorporated into the equation to precisely determine the photothermal conversion efficiency η.

2.7. Detection of ROS *in vitro*

The photodynamic activity of the material was determined through quantification of singlet oxygen ($^1O_2$) formation,

a characteristic ROS, using DPBF as a selective optical probe. The experimental protocol involved mixing aliquots (3 mL each) of aqueous solutions containing water, CMC (3%), PDA (40 μg mL^{-1}), and PDA@Ag (40 μg mL^{-1}) separately with 3 mL of DPBF solution (0.0036 g dissolved in 100 mL anhydrous ethanol) for a 15 min light-protected reaction. The supernatant was then collected and irradiated with 808 nm NIR (1.5 W cm^{-2}) for various time intervals (1, 2, 3, 5, 7, and 10 min). The absorbance of the supernatant was recorded at 416 nm using UV-vis spectroscopy to quantify the generation of $^1O_2$.

2.8. Stability of PDA@Ag

The colloidal stability of the PDA@Ag NPs was examined by suspending the NPs in three different media: PBS (pH 7.4), 10% FBS, and DMEM supplemented with 10% FBS. The hydrodynamic diameter and surface charge characteristics of the PDA@Ag NPs in these dispersion media were analyzed through DLS measurements. Triplicate samples were evaluated daily over seven days to monitor temporal variations in nanoparticle stability.

2.9. *In vitro* antibacterial assay

The broad-spectrum antibacterial efficacy of PDA@Ag-CMC/PEGDA MNs against *S. aureus* and *E. coli* was determined by the colony counting technique. MNs containing 40 μg mL^{-1} PDA@Ag were incubated with bacterial suspensions (1×10^6 CFU mL^{-1}) at 37 °C for 2 h.[45,46] The bacterial suspensions were subsequently irradiated with NIR light (808 nm wavelength, 1.5 W cm^{-2} intensity) for 10 min. Then, 100 μL aliquots of each bacterial suspension were uniformly plated onto sterile agar plates. After incubation for 24 h, digital images of the bacterial colonies were obtained, and colony enumeration was performed using an automated colony counting system. The reference and test groups comprised bacterial suspensions treated with PBS, CMC/PEGDA, PDA-CMC/PEGDA, and PDA@Ag-CMC/PEGDA MNs at different concentrations (10, 20, and 40 μg mL^{-1}), with each group evaluated under irradiated and non-irradiated conditions. The antibacterial effectiveness was quantified as the percentage of bacterial inhibition, with triplicate independent experiments performed to determine the mean antibacterial efficacy. The antibacterial efficacy was calculated using the following eqn (4):

$$R = \frac{CCCG - CCEG}{CCCG} \times 100\% \quad (4)$$

Here, R denotes the antibacterial efficacy ratio, CCCG represents the colony-forming unit enumeration from the control group samples, and CCEG represents the colony-forming unit quantification obtained from the experimental group samples.

The antibacterial efficacy of the PDA@Ag-CMC/PEGDA MNs was assessed *via* a bacterial live/dead staining assay. In this assay, SYTO 9 dye, which emits green fluorescence, is used to stain viable bacteria, whereas propidium iodide (PI), which emits red fluorescence, penetrates compromised cell membranes to stain non-viable bacteria. Fluorescence images were subsequently acquired using a confocal laser scanning microscope (Leica Microsystems, Germany, model Leica DMi8). In line with the sample preparation for the previously described plate counting method, growth curves were generated. The bacterial strains were inoculated in liquid medium and adjusted to the initial concentration ($OD_{600} \approx 0.1$–0.15). The leachates of PBS, CMC, PDA-CMC, and PDA@Ag-CMC/PEGDA MNs containing different concentrations of PDA@Ag (10 μg mL^{-1}, 20 μg mL^{-1}, and 40 μg mL^{-1}) were introduced into a 96-well plate (100 μL per well). Next, 100 μL of liquid medium containing a bacterial suspension of 1×10^6 CFU mL^{-1} was added to each well, and the plate was incubated at 37 °C. The OD_{600} was measured at hourly intervals, and the bacterial growth curve was plotted over 12 h based on these optical density readings.

2.10. Skin penetration ability of the MNs

The porcine skin samples used in this study were obtained from commercially sourced pigs aged 6–8 months, with a body weight of 100–130 kg. Fresh dorsal skin was harvested and prepared by depilating the hair with a scraper and excising excess subcutaneous tissue using a surgical scalpel. The resulting skin specimens, maintained at a thickness of 3–4 mm, were reserved for subsequent puncture testing.

To evaluate the skin penetration ability of the MNs, thumb pressure was applied to press PEGDA, RhB-containing PEGDA, and RhB-containing PDA@Ag-CMC-PEGDA MNs vertically into porcine skin. Before conducting the penetration test, the hair on the porcine cadaver skin was removed using a razor, and the subcutaneous fat was excised using a scalpel. The MN patches were pressed onto the skin surface with thumb pressure, and the duration of penetration was recorded. After 2 min of penetration, the patches were carefully removed from the skin surface, and images were captured using a stereomicroscope (model XHU4005, YIZHAN).

2.11. Stability and drug release of the MNs

The effect of MNs on the stability of drugs was investigated using LiH as a model drug. PDA@Ag-LiH-CMC/PEGDA MNs were exposed to an 808 nm NIR laser (1.5 W cm^{-2}) for 10 min. Then, the MNs were immersed in 10 mL of PBS for 24 h, after which the MN patches were removed to obtain the MN extracts. The surface morphology of the MNs after immersion was examined. Additionally, the absorption curve of LiH in the extract of the PDA@Ag-LiH-CMC/PEGDA MNs following 808 nm NIR irradiation was obtained *via* UV-vis spectroscopy. This was compared with the absorption curves of LiH in the extracts of non-irradiated PDA@Ag-LiH-CMC/PEGDA MNs and untreated LiH to evaluate the effects of photothermal treatment and MN synthesis on LiH stability. The absorbance of the extracts from the PDA@Ag-LiH-CMC/PEGDA MNs was measured at 1, 7, 14, 21, and 28 days to assess the long-term stability of the MNs. Additionally, changes in the weight of the MNs and the LiH content at these time points were examined to investigate the effect of time on the drug loading capacity.

To determine the drug release kinetics of LiH from the MNs, PDA@Ag-LiH-CMC/PEGDA MNs were submerged in 10 mL of PBS and maintained at 37 °C in an orbital shaker (Jiangsu Jinyi Instrument Technology Co., Ltd, model SHA-B). At specified time intervals (0, 3, 5, 7, 10, 15, 20, 25, 30, 45 min, and 1, 2, 3 h), 3 mL aliquots were collected and promptly supplemented with equal volumes of new PBS to ensure a consistent total volume. The LiH content in the extracted samples was subsequently quantified *via* ultraviolet-visible spectrophotometry.

2.12. Evaluation of MN biocompatibility

The cytocompatibility of CMC/PEGDA MNs, PDA-CMC/PEGDA MNs, and PDA@Ag-CMC/PEGDA MNs incorporating different PDA@Ag concentrations (10 μg mL^{-1}, 20 μg mL^{-1}, and 40 μg mL^{-1}), along with PDA@Ag (40 μg mL^{-1})-CMC/PEGDA MNs subjected to NIR exposure, was examined *via* cell viability analysis using the CCK-8 method in murine fibroblast (L929) cells. MN extracts were obtained by immersing MNs in 3 mL of complete growth medium for 24 h. The experimental protocol consisted of seeding L929 cells in 96-well plates at 1×10^4 cells per well in 100 μL of culture medium, followed by incubation under standard conditions (37 °C, 5% CO_2) for 24 h. Then, 100 μL aliquots of the corresponding MN extracts were added to each well. After one, two, or three days of culture, 10 μL of CCK-8 reagent was added to each well, followed by incubation for 2 h. Optical density measurements were performed at 450 nm using a microplate spectrophotometer. The absorbance readings for the control and test groups were used as the OD control and OD samples, respectively. The percentages of viable cells were computed using the following eqn (5):

$$\text{Cell survival rate}\% = \frac{(\text{OD sample})}{\text{OD control}} \times 100\% \quad (5)$$

2.13. *In vivo* photothermal performance

The animal experiments were conducted with 6-week-old female Kunming mice. The study was approved by the Institutional Animal Ethics Committee (TACUC) of Xinjiang Medical University. All procedures were performed in strict compliance with the institution's regulations governing laboratory animal welfare. The dorsal hair of six-week-old female Kunming mice was removed, after which they were randomized into four experimental cohorts. Cohort 1, designated the negative control, remained untreated after depilation. Cohort 2 received PEGDA MNs administered to the denuded skin, Cohort 3 received PDA@Ag/PEGDA MNs, and Cohort 4 received PDA@Ag-CMC/PEGDA MNs. After MN retention for 5 min, the MN arrays were extracted. The irradiation field of the 808 nm NIR laser was calibrated to a 1 cm diameter, with the dorsal skin exposed to a power density of 1.5 W per c for 10 min. Real-time thermal monitoring was performed using an infrared thermographic camera, which captured dorsal temperature fluctuations at intervals of 1 min throughout 10 min of irradiation to assess the *in vivo* photothermal conversion characteristics of the MN systems.

2.14. Statistical analysis

The differences among groups were determined *via* one-way analysis of variance (ANOVA) *via* OriginPro 9.0 software (OriginLab Corporation, Massachusetts, USA). The differences were considered statistically significant at $p < 0.05$. All the data are expressed as the means ± standard deviations (SDs).

3 Results and discussion

3.1. Preparation and characterization of PDA@Ag

Dopamine (DA) has excellent biocompatibility and a good human safety profile. Under weakly alkaline environments, DA molecules self-polymerize to generate PDA, whose surface phenolic groups have reducing capabilities that facilitate the conversion of Ag^+ to Ag^0, resulting in the formation of PDA@Ag NPs (Fig. 1a). The morphological features of the PDA and PDA@Ag NPs were characterized by SEM and TEM, and the PDA NPs appeared as uniform spherical structures with smooth surfaces (Fig. 1b and d), measuring about 340 nm in diameter (Fig. 1g). In contrast, the PDA@Ag NPs presented textured surfaces with well-dispersed metallic NPs embedded within the PDA framework (Fig. 1c and e). These PDA@Ag composites had an average size of 350 nm (Fig. 1h), with elemental mapping confirming the homogeneous distribution of C, N, O, and Ag (Fig. 1f), suggesting the presence of silver NPs (average diameter ~6 nm) on the PDA matrix (Fig. 1i). Zeta potential measurements revealed values of −27.2 mV for PDA and −24.3 mV for PDA@Ag (Fig. 1j), with this shift in potential resulting from the consumption of anionic groups during silver ion reduction, thereby confirming the *in situ* generation of Ag NPs. The UV-vis-NIR absorption spectroscopy data (Fig. 1k) demonstrated that PDA@Ag displayed a prominent plasmon resonance peak at 450 nm, characteristic of silver NPs, along with enhanced NIR absorption at 808 nm, indicating its potential for photothermal applications. X-ray diffraction analysis revealed that PDA has an amorphous halo at 23.1°, whereas PDA@Ag has distinct crystalline peaks at 38.00° (111), 44.16° (200), 64.30° (220), and 77.32° (311), confirming the successful formation of face-centered cubic silver crystals (Fig. 1l). FTIR spectral analysis of PDA@Ag (Fig. 1m) revealed characteristic aromatic stretching vibrations at 1616 cm^{-1} and 1510 cm^{-1}, along with C–O stretching at 1278 cm^{-1}, with peak attenuation suggesting the involvement of PDA in silver reduction. XPS analysis (Fig. 1n and o) revealed characteristic Ag 3d doublets at 367 eV ($3d_{5/2}$) and 373 eV ($3d_{3/2}$), providing additional evidence for the formation of metallic silver. Long-term stability assessment through dynamic light scattering (Fig. 1p and q) revealed minimal variations in hydrodynamic diameter and surface charge when PDA@Ag was dispersed in PBS, 10% fetal bovine serum, or DMEM supplemented with 10% FBS over seven days, indicating excellent physiological stability.

3.2. Preparation and characterization of the PDA@Ag-LiH-CMC/PEGDA MNs

In the field of microneedles (MNs), PEGDA is widely used because it is biocompatible and has excellent mechanical

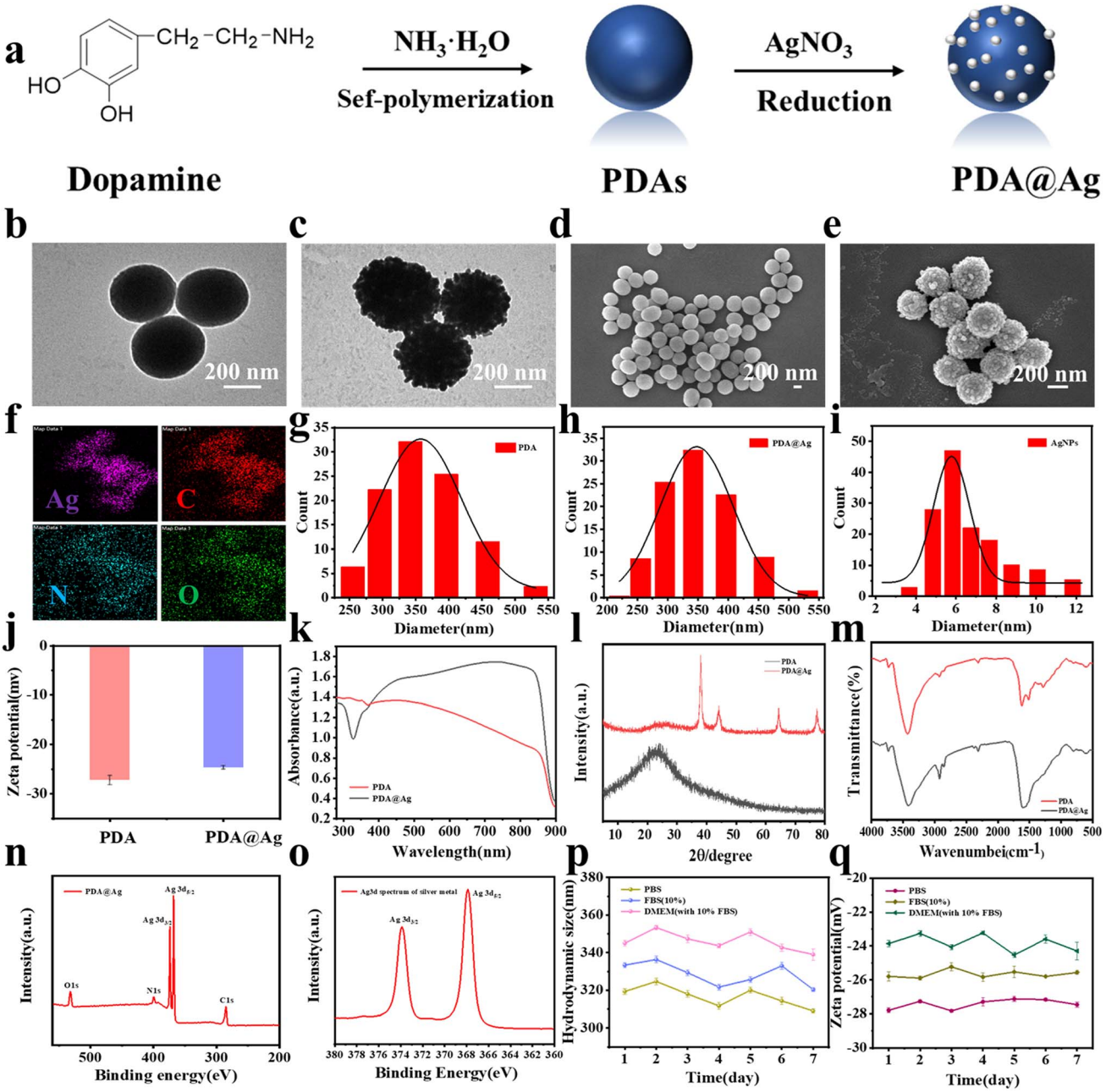

Fig. 1 Physicochemical characterization of PDA and PDA@Ag. (a) Schematic representation of the synthetic procedure for PDA@Ag. (b and c) TEM images of the as-prepared PDA and PDA@Ag samples. (d and e) SEM images of the synthesized PDA and PDA@Ag materials. (f) SEM elemental mapping of the spatial distributions of C, N, O, and Ag in PDA@Ag was performed. (g–i) Size distribution profiles of PDA, PDA@Ag, and surface-deposited Ag NPs. (j) Surface charge characteristics of PDA and PDA@Ag determined by zeta potential measurements. (k) UV-vis-NIR absorption profiles of PDA and PDA@Ag. (l) XRD patterns obtained from PDA and PDA@Ag. (m) FTIR spectra of PDA and PDA@Ag. (n) XPS wide-scan spectrum along with high-resolution (o) Ag 3d spectra. (p and q) Colloidal stability of the PDA@Ag NPs was assessed under physiologically relevant conditions by monitoring the hydrodynamic diameter and surface potential in PBS, 10% fetal bovine serum, and DMEM supplemented with 10% FBS for seven days of observation.

properties. However, pure PEGDA MNs exhibit poor hydrophilicity, and PDA@Ag cannot be uniformly dispersed in the PEGDA solution, leading to phase separation and the inability to synthesize MNs. To enable MNs to load PDA@Ag, we used a method developed previously by our research group to fabricate CMC-coated/PEGDA MNs.[47] By encapsulating PDA@Ag within the CMC coating, we prepared PDA@Ag-CMC/PEGDA MNs, which may be applicable for deep skin treatment. To investigate the ability of MNs to deliver drugs and the effects of high temperatures during photothermal processes on these drugs, we selected LiH as a model drug. LiH was incorporated into the interior of the CMC coating to prepare PDA@Ag-LiH-CMC/PEGDA MNs (Fig. 2a). LiH is a local anesthetic, and the degradation of the CMC coating can lead to the sustained

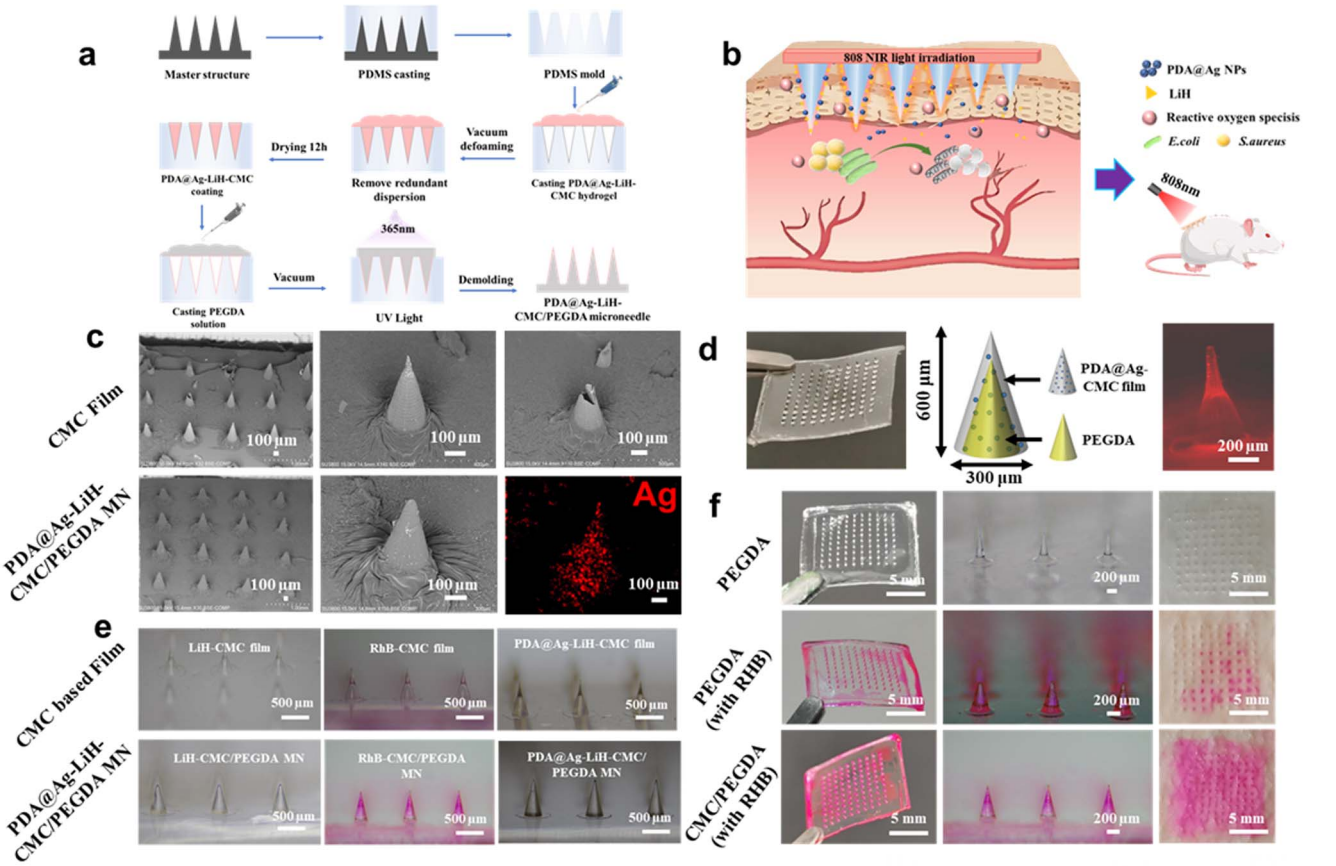

Fig. 2 Characterization of the PDA@Ag-LiH-CMC/PEGDA MNs. (a) Schematic representation of the MN synthesis process. (b) MNs can exhibit synergistic PTT/PDT antibacterial effects. (c) SEM images of the CMC coating and MNs. (d) PDA@Ag-CMC/PEGDA MNs 600 μm tall, 300 μm wide square pyramidal MNs with 700 μm spacing between the needles on a 10 × 10 × 1 mm base. (e) Stereomicroscope images of the CMC-based film and PDA@Ag-LiH-CMC/PEGDA MNs. (f) An MN insertion test was performed using cadaveric porcine skin.

release of LiH, which is useful for postoperative pain management in patients (Fig. 2b). SEM data of the CMC coating and PDA@Ag-LiH-CMC/PEGDA MNs revealed that the CMC coating and the PDA@Ag-CMC/PEGDA MNs were conical. The cross-section of the CMC coating was hollow (S1, S7), indicating that the PDMS mold could synthesize the CMC coating. The presence of Ag on the surface of the composite MNs confirmed that PDA@Ag was loaded onto the CMC/PEGDA MNs (Fig. 2c). The PDA@Ag-CMC/PEGDA MN array consisted of 100 (10 × 10) needles, each with a pyramidal tip having a basal diameter of 300 μm and a height of 600 μm. The PDA@Ag-CMC/PEGDA MN system integrated a dissolvable film with PDA@Ag. The interior of the coating consisted of PEGDA, which serves as the male component. These components were assembled through physical adsorption, with the CMC film adhering to the MN array. RhB was used to visualize the film distribution within the MN patch. As illustrated in Fig. 2d, strong red fluorescence was detected on the surface of the MNs, confirming that RhB was loaded onto the film-coated MNs. Digital photographs and stereomicroscope images of the MNs confirmed the SEM data, both revealing conical shapes. The PDA@Ag-CMC coating and PDA@Ag-CMC/PEGDA MNs had a brownish-yellow color, which indicated that PDA@Ag was incorporated into the coated MNs (Fig. 2e). To assess the distribution of the model drug on the MNs and their skin-piercing performance, RhB was used as the model drug. MNs made from PEGDA, RhB-PEGDA, and RhB-PDA@Ag-LiH-CMC/PEGDA were inserted into cadaver porcine skin for 5 min. After the patches were removed, spots corresponding to the MN array were visible at the insertion sites, with a piercing rate of 100% for all three types, Furthermore, H&E staining further revealed that the microneedles penetrated the stratum corneum to a depth of about 400 μm (S2), indicating that the MNs had satisfactory mechanical strength. The red spots on the skin after piercing with the RhB-PEGDA MNs were uneven, suggesting an uneven distribution of RhB in the PEGDA MNs. In contrast, the red spots on the skin after piercing with RhB-PDA@Ag-LiH-CMC/PEGDA MNs were highly uniform and presented the most intense red color, indicating a very uniform distribution of RhB in the coating. This uniformity suggests that the CMC coating had adequate hydrophilicity, which could increase the drug release rate (Fig. 2f).

3.3. Photothermal performance of the PDA@Ag NPs

We found that PDA@Ag exhibited strong NIR absorption characteristics, probably due to π–π* electronic transitions in the PDA polymeric structure. The photothermal behavior of the

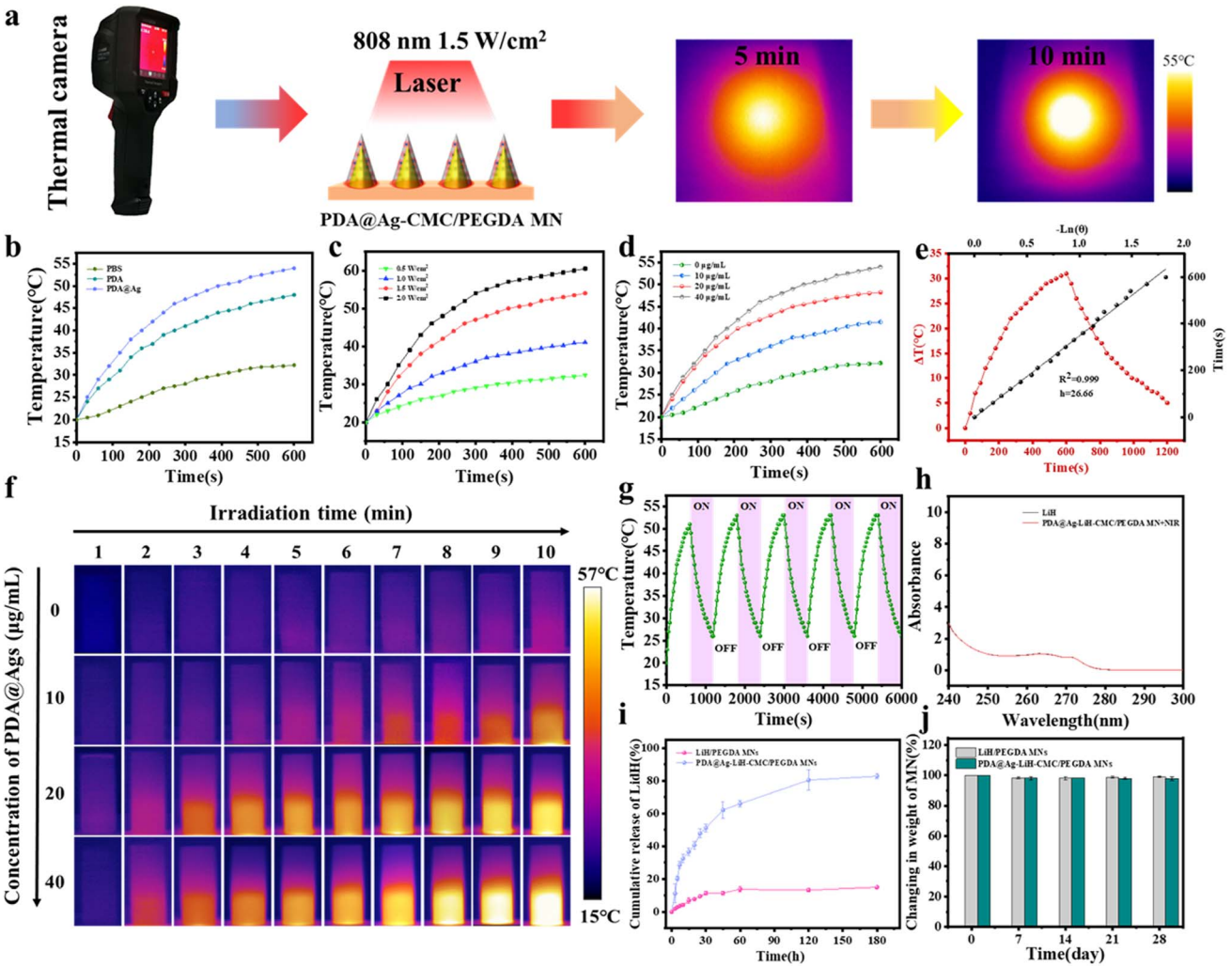

Fig. 3 Physicochemical characterization of the PDA@Ag NPs. (a) Schematic representation of the experimental configuration for photothermal heating of composite MN arrays under 808 nm NIR irradiation at a power density of 1.5 W cm^{-2}, demonstrating the photothermal properties of PDA@Ag and the drug delivery capability of the PDA@Ag-LiH-CMC/PEGDA MNs. (b) Temporal temperature profiles of the PBS control, PDA (40 μg mL^{-1}), and PDA@Ag (40 μg mL^{-1}) solutions during 808 nm NIR irradiation (1.5 W cm^{-2}). (c) Time-dependent temperature variations of PDA@Ag (40 μg mL^{-1}) solutions exposed to different irradiation intensities (0.5, 1.0, 1.5, and 2.0 W cm^{-2}). (d) Photothermal heating profiles and corresponding infrared thermographic images of PDA@Ag solutions at different concentrations (0, 10, 20, and 40 μg mL^{-1}) under 808 nm NIR irradiation (1.5 W cm^{-2}). (e) Heating-cooling cycles of the PDA@Ag aqueous dispersion (40 μg mL^{-1}, 1 mL) during 808 nm laser irradiation (1.5 W cm^{-2}), with cooling phase data used for linear fitting. (f) Real-time photothermal image of PDA@Ag (40 μg mL^{-1}). (g) Photothermal stability of PDA@Ag. (h) UV-vis-NIR spectra of LiH without any treatment and LiH released from PDA@Ag-LiH-CMC/PEGDA MNs. (i) *In vitro* drug release curves of LiH/PEGDA MNs and PDA@Ag-LiH-CMC/PEGDA MNs in a PBS solution. (j) The mass changes of LiH-loaded microneedles at different storage times.

PDA@Ag-CMC/PEGDA MNs was investigated under 808 nm NIR illumination (Fig. 3a). When exposed to an 808 nm laser at 1.5 W cm^{-2}, the temperature of the PDA@Ag-CMC/PEGDA MNs increased progressively, confirming that the photothermal activity within the MN matrix was maintained. Solution-phase studies were performed to systematically characterize the photothermal performance of PDA@Ag. During 10 min of 808 nm laser irradiation (1.5 W cm^{-2}), the PDA@Ag solution temperature increased from 20 °C to 54 °C, outperforming the PDA solution, which reached only 47 °C (Fig. 3b). Compared with PDA, PDA@Ag showed superior photothermal conversion capability, with a calculated efficiency of 26.66% (Fig. 3e). The photothermal response of PDA@Ag was power density dependent, with maximum heating (60 °C) at 2.0 W cm^{-2} and minimum heating (32 °C) at 0.5 W cm^{-2} (Fig. 3c). Under standard 808 nm NIR irradiation (1.5 W cm^{-2}), the photothermal effect of PDA@Ag was concentration dependent, with solutions at 0, 10, 20, and 40 μg mL^{-1} reaching 32 °C, 41 °C, 48 °C, and 54 °C, respectively (Fig. 3d and f). The photothermal stability of PDA@Ag (40 μg mL^{-1}) was also assessed over five laser ON/OFF cycles. During the fifth heating cycle, the maximum temperature attained by PDA@Ag was 51 °C, which indicated the excellent photostability of the PDA@Ag NPs (Fig. 3g). These findings suggested that PDA@Ag serves as a functional nanoparticle with robust photothermal properties. To assess the effect of the MN fabrication process on the stability of active

pharmaceuticals, we used LiH as a model compound. We also examined the UV-vis-NIR spectra of LiH released from the MNs and compared them to those of untreated LiH. Both untreated LiH and LiH released from the MNs exhibited absorption at about 263 nm. The consistency in the absorption peak position and the absence of a decrease in absorbance suggested that the LiH within the MNs remained intact (Fig. 3h). Using a standard curve derived from the absorbance of LiH at different concentrations, we determined that the drug loading per MN patch was 78 μg (S3–S4). The drug release profile of the PDA@Ag-LiH-CMC/PEGDA MNs reached 83% release within 3 h, whereas that of the LiH/PEGDA MNs reached only 15% release during the same timeframe. These findings showed that the CMC coating enhances the drug release kinetics of PEGDA MNs (Fig. 3i). To evaluate long-term stability, LiH/PEGDA and PDA@Ag-LiH-CMC/PEGDA MNs were stored at 4 °C, and their masses were measured at different intervals (0, 7, 14, 21, and 28 days). These results indicated that the mass of the MNs remained stable throughout the storage period (Fig. 3j). PDA@Ag-LiH-CMC/PEGDA MNs stored at 4 °C for 0, 7, 14, 21, or 28 days were subsequently immersed in PBS for 6 h to determine their drug-loading capacity. The results indicated that the drug-loading capacity remained above 96%, indicating the high stability of the PDA@Ag-LiH-CMC/PEGDA MNs during storage (S5). To confirm the drug release ability of the CMC/PEGDA MNs, RhB was selected as a model drug, and RhB-CMC/PEGDA MNs were generated. These MNs were inserted into simulated skin composed of agarose hydrogel (1.4 wt%). After the MN patch was removed, red spots were found at the puncture sites (S6). Before insertion, the MNs were red and conical. However, after insertion, the MN needles were smaller and had blunted tips (S7), collectively demonstrating the capacity of the MNs for drug loading and release.

3.4. Photodynamic and photostability of the PDA@Ag NPs

The synergistic photothermal/photodynamic antibacterial effects were evaluated by immersing PDA@Ag-CMC/PEGDA MNs in PBS for 6 h to obtain the extraction solution, which produces ROS under 808 nm NIR irradiation. The production of $^1O_2$ was monitored using DPBF as a molecular probe (Fig. 4a) on the basis of the characteristic decrease in the absorbance of DPBF at 416 nm after oxidation by $^1O_2$ (Fig. 4b).[48] Control experiments revealed negligible changes in DPBF absorbance for water, CMC, and PDA solutions during prolonged exposure to light (Fig. 4b–d), confirming their limited $^1O_2$ production capacity. However, the PDA@Ag solutions significantly decreased the DPBF absorbance upon irradiation (Fig. 4e), demonstrating efficient $^1O_2$ generation. Quantitative analysis revealed $^1O_2$ generation rates of about 89% and 82% for PDA, whereas rates of 87% and 72% were reported for PDA@Ag under identical irradiation conditions (Fig. 4f). These findings showed that, compared with PDA alone, PDA@Ag results in greater production of ROS. To characterize the reactive species further, we used DMPO as a spin trap to identify $^{\bullet}OH$ and $^{\bullet}O_2^-$ production from the PDA@Ag samples. ESR analysis revealed no $^{\bullet}OH$ signals in the unirradiated samples (0 min), whereas distinct $^{\bullet}OH$ peaks with characteristic intensity ratios were found after 10 min of NIR irradiation at 808 nm (Fig. 4g). Similarly, $^{\bullet}O_2^-$ signals were detected exclusively in the irradiated PDA@Ag samples (Fig. 4h), with the characteristic ESR spectrum confirming efficient $^{\bullet}O_2^-$ generation through photodynamic processes. These observations revealed substantial $^{\bullet}OH$ and $^{\bullet}O_2^-$ production under NIR excitation. ICP-MS measurements revealed that the Ag content in the nanospheres was 77.7 wt% (Table S1). Cytotoxicity evaluation *via* CCK-8 assays revealed that L929 fibroblasts maintained >92% viability after 72 h of exposure to PDA@Ag-CMC/PEGDA MN extracts (0.5 cm^2, 8 μg Ag per mg film), which was comparable to that of untreated controls (Fig. 4i). The cell viability remained above 91% even after 10 min of NIR irradiation (1.5 W cm^{-2}). Confirming excellent biocompatibility for potential clinical implementation (S8).

3.5. *In vitro* antibacterial activity of the PDA@Ag-CMC/PEGDA MNs

The broad antibacterial efficacy of the PDA@Ag-CMC/PEGDA MNs was assessed against two representative skin infection pathogens: Gram-negative *E. coli* and Gram-positive *S. aureus* (Fig. 5a). Quantitative evaluation *via* colony counting assays revealed the synergistic antibacterial effects of PDA@Ag-CMC/PEGDA MNs with or without exposure to NIR light at 808 nm (Fig. 5b). Without photothermal activation, the rates of *E. coli* inhibition by PBS, CMC/PEGDA, PDA-CMC/PEGDA, and increasing concentrations of PDA@Ag (10, 20, and 40 μg mL^{-1}) were 0%, 40.66%, 58.95%, 66.38%, 78.67%, and 95.93%, respectively. When combined with NIR irradiation, the antibacterial performance improved significantly, showing inhibition rates of 7.5% (PBS + NIR), 63.27% (CMC/PEGDA + NIR), and 68.58% (PDA-CMC + NIR) and 72.07%, 96.37%, and 99% for the corresponding PDA@Ag concentration groups, respectively (Fig. 5c). The bactericidal effects against *S. aureus* were quantitatively assessed after treatment with PBS, CMC/PEGDA, PDA-CMC/PEGDA, and PDA@Ag-CMC/PEGDA containing different concentrations of PDA@Ag (10, 20, and 40 μg mL^{-1}), with inhibition rates of 0%, 38.70%, 58.23%, 61.05%, 75.83%, and 94.86%, respectively. After exposure to NIR irradiation, the corresponding treatment groups (PBS + NIR, CMC/PEGDA + NIR, PDA-CMC + NIR, and PDA@Ag^+NIR at increasing concentrations) presented greater antibacterial efficacy, with inhibition rates reaching 7%, 58.35%, 69.58%, 71.74%, 95.28%, and 98.37%, respectively (Fig. 5d). These findings indicated a dose-dependent antibacterial response of PDA@Ag-CMC/PEGDA MNs against *S. aureus*, with NIR irradiation providing significant additional bactericidal enhancement.

To determine the broad-spectrum antibacterial performance *in vitro*, CMC/PEGDA, PDA-CMC/PEGDA, and PDA@Ag-CMC/PEGDA MNs containing different doses of PDA@Ag were incubated with *E. coli* or *S. aureus* with/without exposure to NIR irradiation at 808 nm. Bacterial viability staining revealed that after incubation for 12 h, the mortality of both bacterial strains increased with increasing concentrations of PDA@Ag. At equivalent PDA@Ag concentrations, the NIR-treated groups

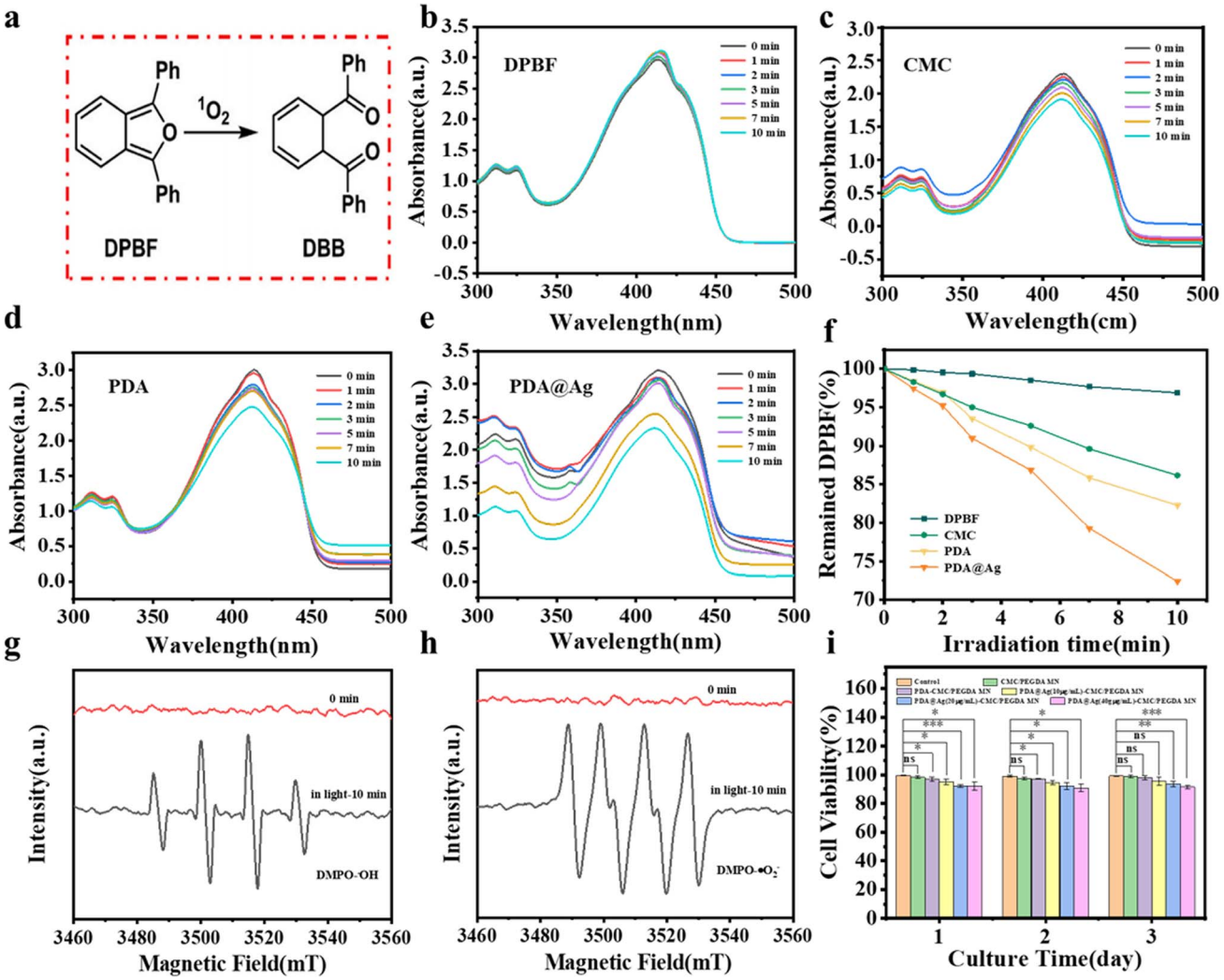

Fig. 4 Assessment of the ROS and biocompatibility of the MNs. (a) Schematic representation of DPBF utilization as a specific indicator of singlet oxygen ($^1O_2$). UV-vis absorption spectra of DPBF in (b) water, (c) CMC, (d and e) PDA, and PDA@Ag under irradiation (808 nm, 1.5 W cm^{-2}) at different time points. (f) Decay profiles of the relative absorption of DPBF at 420 nm across different irradiation durations for each group. (g) ESR spectra indicating hydroxyl radical ($^{\bullet}$OH) generation by PDA@Ag. (h) ESR spectra demonstrating superoxide anion ($^{\bullet}O_2^-$) production by PDA@Ag. (i) Viability of L929 fibroblasts after 24 h of exposure to different MN formulations.

presented greater bactericidal activity (S9). The quantitative antibacterial rates were correlated with the results of viability staining. The control groups (CMC/PEGDA and PDA/PEGDA MNs) presented minimal bacterial suppression in viability assays, confirming the excellent broad antibacterial capacity of the PDA@Ag-CMC/PEGDA MN arrays. For quantitative assessment, different MN formulations were incubated in bacterial suspensions with/without NIR treatment, and growth inhibition was quantified *via* optical density measurements (Fig. 5e–j). Compared with the untreated control, all the tested Gram-negative and Gram-positive bacteria presented distinct growth inhibition patterns after treatment with CMC/PEGDA, PDA-CMC/PEGDA, or PDA@Ag-CMC/PEGDA MNs. The surface plasmon resonance phenomenon exhibited by the PDA-encapsulated Ag NPs improved the separation yield of the photoinduced charge carriers. The liberated electrons subsequently reduce adsorbed molecular oxygen to catalyze ROS production, inducing oxidative damage through lipid peroxidation of cellular membranes, destruction of subcellular components, and DNA degradation, ultimately causing bacterial lethality. Additionally, the sharp tips of the PDA@Ag-CMC/PEGDA MNs mechanically compromised the structural integrity of the bacterial biofilms, promoting deeper penetration of antibacterial agents. Our results suggest that this platform allows spatially controlled ROS production within targeted tissue regions for precision antibacterial therapy. The combined PTT/PDT strategy, which uses NIR-triggered membrane hyperthermia and ROS-induced oxidative stress, confers exceptional bactericidal performance to the MN system (Fig. 5k).

3.6. Delivery of PDA@Ag to mouse skin

We used BALB/C mice as the animal model and anesthetized them with 1% sodium pentobarbital. The hair on the backs of

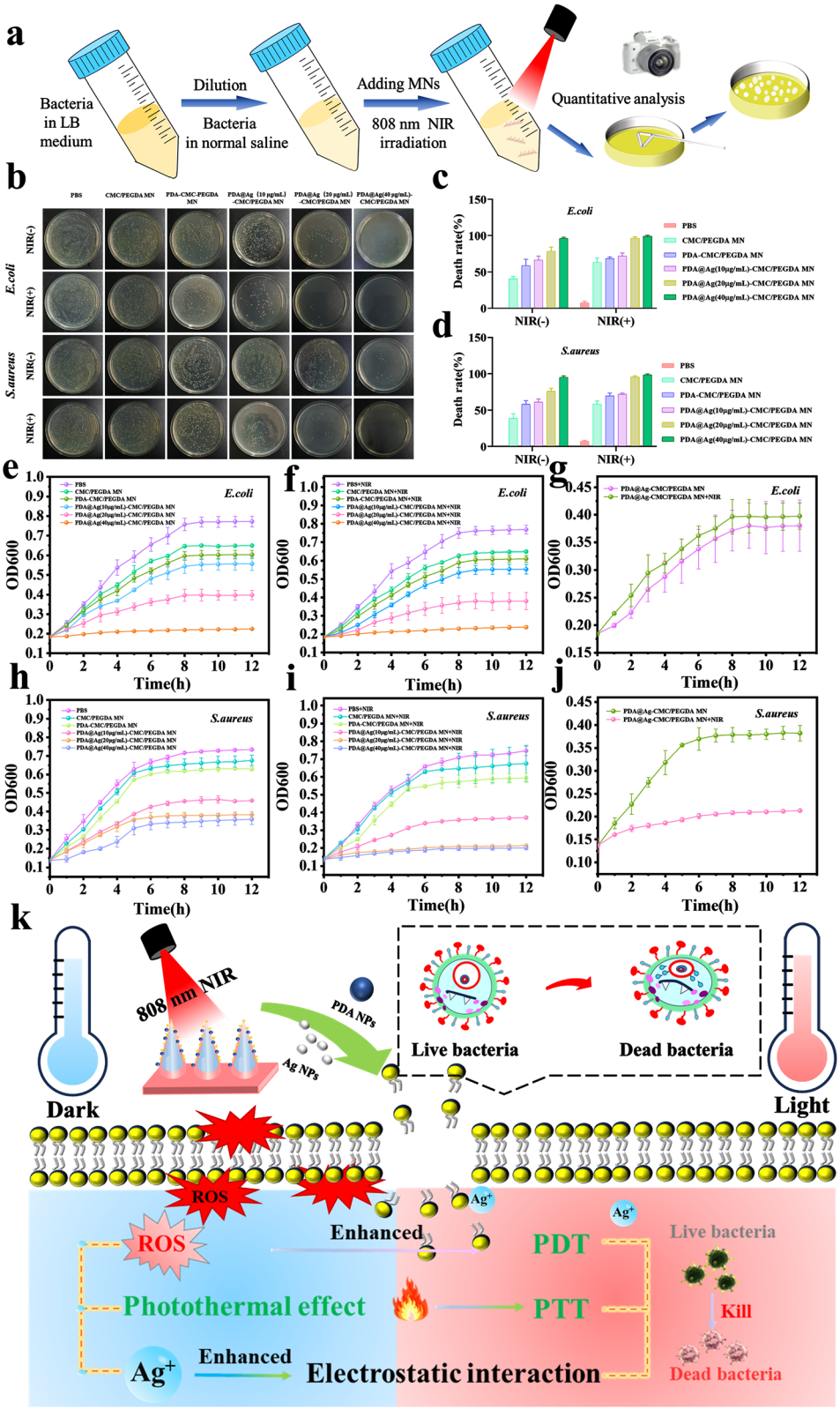

Fig. 5 Antibacterial evaluation. (a) Experimental design for photothermal antibacterial assessment. (b) Bacterial colony formation of *E. coli* and *S. aureus* after treatment with PBS, CMC/PEGDA, PDA-CMC/PEGDA, or PDA@Ag-CMC/PEGDA containing different concentrations of PDA@Ag (10, 20, and 40 μg mL^{-1}), with or without 808 nm laser irradiation (1.5 W cm^{-2}, 10 min), followed by incubation for 12 h. (c and d) Quantitative bactericidal efficiency against *E. coli* and *S. aureus*. (e–g) Bacterial growth curves of various MNs without or with 808 nm NIR irradiation: the OD value of media containing *E. coli*. (h–j) Bacterial growth curves of various MNs without or with 808 nm NIR irradiation: the OD value of media containing *S. aureus*. (k) Proposed mechanism of PDA@Ag-CMC/PEGDA MN-mediated antibacterial action.

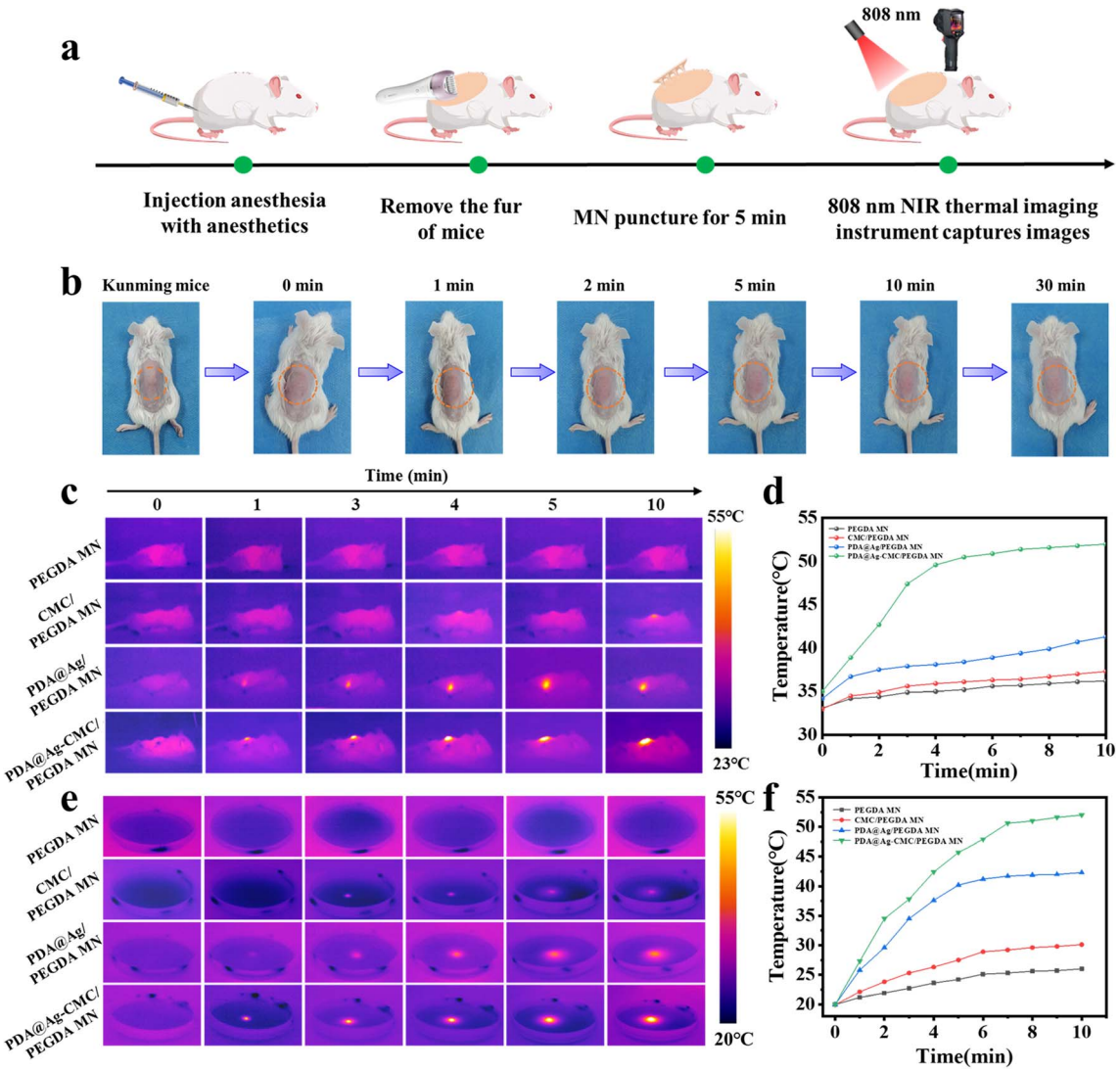

Fig. 6 Evaluation of the NIR-activated photothermal performance of the PDA/Ag composites in biological and simulated environments. (a) Experimental design of the murine model. (b) Temporal progression of skin recovery following removal of the MN patch. (c and d) Infrared thermal images and corresponding temperature increases at the puncture sites of murine skin treated with PEGDA, CMC/PEGDA, PDA@Ag/PEGDA, or PDA@Ag-CMC/PEGDA after exposure to NIR irradiation (808 nm, 1.5 W cm^{-2}) at specified time intervals. (e and f) Infrared thermal images and corresponding temperature increases at the puncture sites of the agarose hydrogel under the same NIR irradiation.

the mice was removed using depilatory cream, and the MNs were inserted into the skin for 5 min. We examined skin recovery after treatment (Fig. 6b) or PDA@Ag delivery (Fig. 6a). The puncture sites, initially exhibiting an erythematous appearance, showed progressive contraction with complete resolution within 30 min, indicating rapid tissue recovery from mechanical deformation. This accelerated healing response is clinically advantageous for minimizing the risk of infection associated with transdermal drug delivery *via* MN systems. The mouse skin has a thinner epidermis (only 2–3 layers of keratinocytes, with a total thickness of about 10–20 μm), a thin stratum corneum, and high transdermal absorption efficiency. In contrast, human skin has a thicker epidermis (about 50–100 μm). We inserted CMC/PEGDA MNs into the skin surface of a human (woman, 33 years old) for 2 min, and after removing the patch, the puncture holes contracted and disappeared within 1 h. This occurred probably because mouse skin is pink, whereas Asian skin is yellow, making the red spots more visible on human skin (S10). Distinct fluorescence signals were detected at most MN penetration sites, confirming the effective transdermal delivery of the PDA@Ag NPs (Fig. 6c). To systematically evaluate the distribution of PDA@Ag *in vivo*, different MN formulations were administered to depilated mouse skin through gentle digital pressure application for 5 min. Real-time thermal monitoring during exposure to an NIR laser at 808 nm was performed using infrared thermography. The PDA@Ag-CMC/PEGDA MN group exhibited a maximal photothermal response at the application sites, achieving a surface temperature of 52 °C after 10 min of NIR irradiation (808 nm). In contrast, the temperature variations in the PEGDA, CMC/

PEGDA, and PDA@Ag/PEGDA MN-treated groups remained minimal (Fig. 6d). The mouse skin surface has a lower water content, and the PDA@Ag/PEGDA MNs delivered less PDA@Ag on the mouse skin surface, which may lead to less drug release on the surface of living animals and, thus, a lower skin surface temperature during photothermal treatment. To verify this, we sequentially inserted the above MNs into simulated skin made of agarose hydrogel (Fig. 6e). The hydrogel punctured by PDA@Ag-CMC/PEGDA MNs presented the greatest increase in temperature, indicating that these MNs delivered PDA@Ag at the fastest rate. The temperature curve on the surface of the hydrogel showed that the increase in the temperature of the hydrogel punctured by the PDA@Ag/PEGDA MNs was greater than that in the mouse skin, which may be due to the higher water content in the hydrogel, which allowed the faster release of PDA@Ag from the PDA@Ag/PEGDA MNs (Fig. 6f). The temperature increase effect of the hydrogel punctured by the PDA@Ag-CMC/PEGDA MNs was similar to that of the mouse skin, indicating that the PDA@Ag-CMC/PEGDA MNs had a good drug release rate even in mouse skin with a low water content. This animal study revealed that the soluble CMC content accelerated the transdermal release of PDA@Ag.

4 Conclusions

In this study, we developed a system comprising PDA@Ag NPs and CMC film-coated PEGDA MNs, which exhibited favorable biocompatibility for antibacterial applications. These findings confirmed the successful synthesis of Ag NPs *via in situ* polymerization within the PDA matrix. The integration of PDA@Ag enhanced the photothermal and photodynamic properties of the composite MNs. The combination of CMC/PEGDA MNs with PDA@Ag demonstrated the capacity to generate ROS with potent bactericidal activity, highlighting that they may be used in deep-level antibacterial therapy. The PDA@Ag-LiH-CMC/PEGDA MNs exhibited antibacterial effects and facilitated the sustained release of LiH in target tissues, thereby increasing the local drug concentration while minimizing systemic side effects. We described an integrated therapeutic methodology and proposed a composite MN system as a platform for antibacterial treatment and wound pain management.

Author contributions

Y. G.: conceptualization, methodology, investigation, data curation, validation, visualization, writing – original draft, writing – review & editing, funding acquisition, supervision, project administration. H. H.: investigation, data curation, validation, visualization. J. L.: conceptualization. N. W.: investigation, data curation. H. G.: investigation, data curation. Y. W.: writing – original draft, writing – review & editing, funding acquisition, supervision. All authors have read and agreed to the published version of the manuscript.

Conflicts of interest

The authors declare no competing financial interest.

Data availability

The data supporting this article are included within the main text or the supplementary information (SI). Additional data are available from the authors upon request.

Supplementary information: confocal images of RhB-CMC/PEGDA MNs, histological sections of porcine skin before and after penetration by MNs, UV absorption spectra of LiH, the standard curve of LiH, drug stability of PDA@Ag-LiH-CMC/PEGDA MNs under various storage times, RhB-CMC/PEGDA MNs applied to agarose hydrogel-simulated skin, stereomicroscopy images of RhB-CMC/PEGDA MNs before and after insertion into agarose hydrogel-simulated skin, the viability of the cells treated with the extracting solution of PDA@Ag-CMC/PEGDA MNs, irradiated with or without an 808 nm laser at 1.5 W cm^{-2} for 10 min, fluorescence microscopy images showing bacterial viability (DMAO, green: live; PI, red: dead) for both bacterial strains, recovery of the human skin over time after the removal of the CMC/PEGDA MNs patch, ICP data for Ag in PDA@Ag nanoparticles. See DOI: **https://doi.org/10.1039/d5ra04189a**.

Acknowledgements

This project was funded by Xinjiang Normal University Research Foundation for Doctoral Program (XJNUBS2307). National Natural Science Foundation of China (No. 52362039). Xinjiang Key Laboratory of Energy Storage and Photo electrocatalytic Materials, the Tianshan Talent Training Program (No. 2023TSYCCX0096). Xinjiang Normal University Student Innovation and Entrepreneurship Training Program (X202410762106). Xinjiang Normal University Graduate Student Research and Innovation Project (XSY202501021).

References

1 Y. Zhang, X. Hu, J. Shang, W. Shao, L. Jin, C. Quan and J. Li, *Theranostics*, 2022, **12**, 5995.
2 Y. Hu, M. Ding, X. Lv, J. Jiang, J. Zhang and D. Yang, *Adv. Healthcare Mater.*, 2024, **13**, 2402240.
3 J. Zhang, H. Dong, B. Liu and D. Yang, *Small*, 2025, **21**, 2408543.
4 C. Wang, X. Wei, L. Zhong, C. Chan, H. Li and H. Sun, *J. Am. Chem. Soc.*, 2025, **147**, 12361–12380.
5 M. Bassetti, G. Poulakou, E. Ruppe, E. Bouza, S. J. Van Hal and A. Brink, *Intensive Care Med.*, 2017, **43**, 1464–1475.
6 P. Manivasagan, T. Thambi, A. Joe, H. W. Han, S. H. Seo, Y. J. Jeon, J. Conde and E. S. Jang, *Prog. Mater. Sci.*, 2024, **144**, 101292.
7 N. Yadav and V. S. Chauhan, *Adv. Colloid Interface Sci.*, 2024, **333**, 103282.
8 J. Huo, Q. Jia, H. Huang, J. Zhang, P. Li, X. Dong and W. Huang, *Chem. Soc. Rev.*, 2021, **50**, 8762–8789.
9 S. Liu, Y. Feng, Q. Meng, X. Wang, Y. Liang, G. Yang, Y. Su, K. Zhang, C. Qi and K. Cai, *Chem. Eng. J.*, 2025, **503**, 158108.
10 X. Zhou, T. Chen, T. Ma, L. Yan, H. Wei, S. Liu, Z. Dai, Z. Xie, J. Deng and S. Tao, *Adv. Healthcare Mater.*, 2023, **12**, 2301206.

11 K. Yang, S. Zhao, B. Li, B. Wang, M. Lan and X. Song, *Coord. Chem. Rev.*, 2022, **454**, 214330.
12 R. Ge, P. Yan, Y. Liu, Z. Li, S. Shen and Y. Yu, *Adv. Funct. Mater.*, 2023, **33**, 2301138.
13 M. Du, X. He, D. Wang, Z. Jiang, X. Zhao and J. Shen, *Acta Biomater.*, 2024, **179**, 300–312.
14 B. Zheng, Q. Li, L. Fang, X. Cai, Y. Liu, Y. Duo, B. Li, Z. Wu, B. Shen and Y. Bai, *Nat. Commun.*, 2024, **15**, 8947.
15 S. Yang, Y. Xu, M. Zhu, Y. Yu, W. Hu, T. Zhang and J. Gao, *Adv. Mater.*, 2025, **37**, 2411112.
16 Y. Han, X. Qin, W. Lin, C. Wang, X. Yin, J. Wu, Y. Chen, X. Chen and T. Chen, *Nano-Micro Lett.*, 2025, **17**, 132.
17 T. Wen, Y. Zhao, Y. Fu, Y. Chen, X. Li, C. Shi, D. Xian, W. Zhao, D. Yang and C. Lu, *Mater. Today Bio*, 2024, **29**, 101327.
18 T. Peng, Y. Chen, X. Luan, W. Hu, W. Wu, B. Guo, C. Lu, C. Wu and X. Pan, *Bioact. Mater.*, 2025, **45**, 274–300.
19 Y. Liu, K. Liu, L. Lei, Q. Wang, X. Wang, X. Meng, Q. Liu, J. Du, L. Zhang and M. Nazaré, *ACS Appl. Mater. Interfaces*, 2024, **17**, 1–12.
20 R. Xie, D. Fan, Y. Fang, T. Zhu, H. Li, Y. Yin, X. Liu, Y. Ma, F. Chen and W. Zeng, *Adv. Healthcare Mater.*, 2025, 2405190.
21 R. Cai, J. Zhao, P. Zhou, X. Ma, C. Zhang, Z. Wu, L. Hu, Y. Hu, Y. Chen and C. Huang, *Mater. Today Bio*, 2025, **31**, 101605.
22 F. R. Xu, G. L. Zhang, K. Zhang, P. Chen, Q. Wang, Y. Pan, B. Z. Tang and H. T. Feng, *Aggregate*, 2025, **6**, e699.
23 M. Xing, W. Qian, K. Ye, H. Zhang, J. Feng, X. Liu and J. Qiu, *Biomaterials*, 2025, **320**, 123251.
24 Y. Gao, H. Huo, R. Zhang, H. Gao, Y. Liu and Y. Wang, *ACS Appl. Mater. Interfaces*, 2024, **16**, 70339–70351.
25 C. Zhang, P. Yang, J. Li, S. Cao, Y. Liu and J. Shi, *Dalton Trans.*, 2024, **53**, 14315–14324.
26 P. Wang, Q. Xiang, Z. Fu, C. Li, H. Yang, J. Zhang, X. Luo and L. Chen, *J. Hazard. Mater.*, 2025, **492**, 138279.
27 S. Tang and J. Zheng, *Adv. Healthcare Mater.*, 2018, **7**, 1701503.
28 S. Ali, A. Bahadur, A. Hassan, S. Ahmad, W. Shah and S. Iqbal, *Chem. Eng. J.*, 2025, **507**, 160470.
29 M. Cui, S. Li, X. Ma, J. Wang, X. Wang, N. E. Stott, J. Chen and J. Zhu, *Int. J. Biol. Macromol.*, 2024, **256**, 128088.
30 A. R. Rafieerad, A. R. Bushroa, A. Amiri, K. Kalaiselvam, K. M. Vellasamy and J. Vadivelu, *J. Hazard. Mater.*, 2018, **360**, 132–140.
31 C. Zhang, K. Zhang, Y. Wang, Y. Ye, T. Kong, Y. Li, N. Zhao and F. Xu, *Adv. Funct. Mater.*, 2025, 2505906.
32 Q. Dai, R. Jia, H. Li, J. Yang and Z. Qin, *ACS Sustain. Chem. Eng.*, 2024, **12**, 1388–1404.
33 N. Chokesawatanakit, P. Jutakridsada, S. Boonlue, J. T. N. Knijnenburg, P. C. Wright, M. Sillanpää and K. Kamwilaisak, *J. Environ. Chem. Eng.*, 2021, **9**, 105843.
34 X. Qi, Y. Huang, S. You, Y. Xiang, E. Cai, R. Mao, W. Pan, X. Tong, W. Dong and F. Ye, *Adv. Sci.*, 2022, **9**, 2106015.
35 Y. Wu, Y. Lin, Y. Chen, H. Fan, J. Zhang, J. Li, W. Lin, G. Yi and X. Feng, *Int. J. Biol. Macromol.*, 2024, **259**, 129266.
36 M. Ding, Y. Zhang, X. Li, Q. Li, W. Xiu, A. He, Z. Dai, H. Dong, J. Shan and Y. Mou, *Small*, 2024, **20**, 2400927.
37 M. Ji, F. Li, J. Li, J. Li, X. Wang, C. Zhang, S. Peng and J. Man, *Int. J. Biol. Macromol.*, 2024, **278**, 134714.
38 Y. Geng, H. Xue, Z. Zhang, A. C. Panayi, S. Knoedler, W. Zhou, B. Mi and G. Liu, *Carbohydr. Polym.*, 2023, **305**, 120555.
39 M. Pourmadadi, E. Rahmani, A. Shamsabadipour, A. Samadi, J. Esmaeili, R. Arshad, A. Rahdar, F. Tavangarian and S. Pandey, *Process Biochem.*, 2023, **130**, 211–226.
40 Z. Shariatinia, *Int. J. Biol. Macromol.*, 2018, **120**, 1406–1419.
41 A. Harugade, A. P. Sherje and A. Pethe, *React. Funct. Polym.*, 2023, **191**, 105634.
42 J. H. Ryu, P. B. Messersmith and H. Lee, *ACS Appl. Mater. Interfaces*, 2018, **10**, 7523–7540.
43 L. Wang, K. Song, C. Jiang, S. Liu, S. Huang, H. Yang, X. Li and F. Zhao, *Adv. Healthcare Mater.*, 2024, **13**, 2401451.
44 Y. Mao, X. Zhang, Y. Sun, Z. Shen, C. Zhong, L. Nie, A. Shavandi, K. E. Yunusov and G. Jiang, *Biomed. Microdevices*, 2024, **26**, 9.
45 L. He, D. Di, X. Chu, X. Liu, Z. Wang, J. Lu, S. Wang and O. Zhao, *J. Controlled Release*, 2023, **363**, 180–200.
46 Z. P. Li, S. You, R. Mao, Y. Xiang, E. Cai, H. Deng, J. Shen and X. Qi, *Mater. Today Bio*, 2022, **15**, 100264.
47 Y. Gao, M. Hou, R. Yang, L. Zhang, Z. Xu, Y. Kang and P. Xue, *J. Mater. Chem. B*, 2019, **7**, 7515–7524.
48 H. Luo, H. Xu, H. Zhang, X. Li, Q. Wu and T. Gao, *Carbohydr. Polym.*, 2025, **352**, 123147.